Received: 27 September 2017 | Revised: 12 June 2018 | Accepted: 22 October 2018

DOI: 10.1002/asmb.2431

SPECIAL ISSUE PAPER

WILEY

Nonlocal spatial clustering in automated brain hematoma and edema segmentation

Wei Tu[1] | Linglong Kong[1] | Rohana Karunamuni[1] | Ken Butcher[2] | Lili Zheng[1] | Rebecca McCourt[2]

[1]Department of Mathematical and Statistical Sciences, University of Alberta, Edmonton, Canada

[2]Division of Neurology, University of Alberta, Edmonton, Canada

Correspondence
Wei Tu, Department of Mathematical and Statistical Sciences, University of Alberta, Edmonton T6G 2G1, Canada.
Email: wei.tu@ualberta.ca

Funding information
Natural Sciences and Engineering Research Council of Canada; Canadian Statistical Sciences Institute

Abstract

Hematoma and edema volume are potential predictors of 30-day mortality rate and functional outcome (degree of disability or dependence in daily activities after a stroke) for patients with intracerebral hemorrhage. The manual segmentation of hematoma and edema from computed tomography scans is common practice but a time-consuming and labor-intensive task. Automated segmentation is an appealing alternative, but it is challenging because of the poorly defined boundary between edema and the surrounding healthy brain tissue. There is limited literature on this problem, and we aim to help fill the gap between the theoretical development of segmentation methods and the practical need. Our framework is fully automated and requires no supervision. The method uses nonlocal regularized spatial fuzzy C-means clustering in the initialization stage and the active contour without edges method in the refinement stage. To evaluate it, we used 30 subjects with different sizes, shapes, and locations of hematoma and edema. Compared with the manual segmentation results from two independent raters, our method performs hematoma segmentation well, with an average dice score coefficient of 0.92. Although there is a lack of ground truth in edema segmentation due to the high inter and intrarater variation, our results are comparable with manual segmentation results.

KEYWORDS

active contour without edges, computed tomography, medical image segmentation, nonlocal spatial clustering

1 | INTRODUCTION

Intracerebral hemorrhage (ICH) is a type of intracranial bleed that occurs within the brain tissue or ventricles. In addition, ICH currently has no effective treatment and is estimated to affect over a million people worldwide each year,[1,2] most of whom either die or are seriously disabled.[3] Noncontrast computed tomography (CT) has been the standard imaging modality for the initial evaluation of patients presenting with acute stroke symptoms[4] because it can identify the presence of hemorrhage in the hyperacute phase.

The volume of ICH is the strongest predictor of 30-day mortality and morbidity in patients with spontaneous ICH.[5] The inflammatory response to ICH can cause secondary injuries, including perihematomal edema (PHE).[6] PHE is present

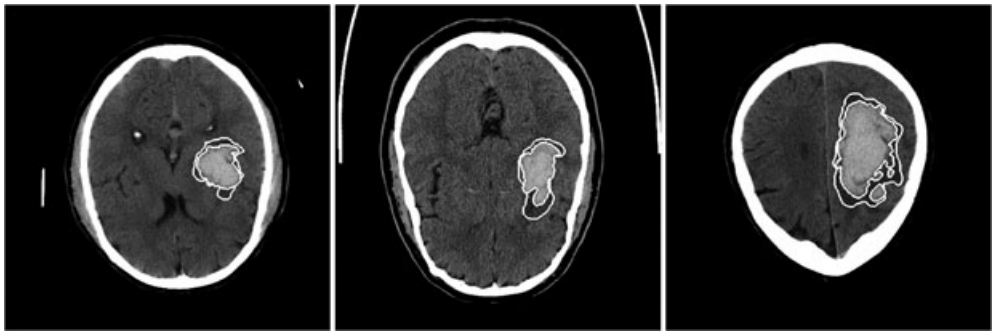

FIGURE 1 Computed tomography scans with hematoma and surrounding edema

in most patients with ICH. Some studies[7,8] have suggested using the relative edema volume (edema volume divided by hematoma volume) as an independent predictor of patients' functional outcome (a score measuring the degree of disability or dependence in daily activities after a stroke). The classical way to measure hematoma and edema volume is manual delineation by an experienced rater. This task is time consuming (about 10 minutes) and labor intensive, but it is considered to be the gold standard.

Manual measurements of hematoma volume are usually accurate, with a low degree of inter and intrarater variation. However, the measurement of edema volume is much more challenging because of the subtle difference from the surrounding healthy brain tissue; the inter and intrarater variation is much higher. In the work of Zimmerman et al,[9] the hematoma and edema volumes measured by two raters on 1144 CT scans were compared. In 84% of the scans, there was a difference of at most 2 mL for the hematoma volume, but the mean differences for the edema volume were roughly 5 to 15 mL. Moreover, 91 scans were reread by the same rater, and the differences between the two hematoma readings were very small ($\leq$ 1 mL), whereas the average differences for the edema readings were more than 3 mL.

An automated segmentation algorithm for hematoma and edema would be fast and efficient as well as objective and consistent. An accurate algorithm could also help physicians to trace longitudinal changes in the hematoma and edema volumes, gaining a better understanding of their development. Figure 1 shows three CT scans of hematoma and the surrounding edema; the contours were drawn by an experienced radiologist. The region inside the inner white circle is hematoma, and the tissue between the two contours is edema. Magnetic resonance imaging (MRI) is considered superior for edema quantification because of the high contrast between the perihematomal hyperintensity and the neighboring brain tissue. However, MRI is not usually an option for patients with ICH because the waiting time is too long, given the instability of their condition.

Most research on brain image segmentation has focused on tumor segmentation. The most frequently studied image modality is MRI, and Gordillo et al[10] provides a review. There is limited literature on the hematoma and edema segmentation of CT scans. One approach[11] uses fuzzy clustering to segment the abnormal tissue, which includes both hematoma and edema, and then a fuzzy expert system to decide the actual segmentation based on the results from the first part and a set of rules. Bardera et al[12] proposed a semiautomated method for brain hematoma and edema segmentation. They first use a region-growing approach to segment hematoma based on the user's seed set, and they then apply a level set approach for the edema segmentation. The initialization stage requires human intervention. Methods for automated hematoma segmentation include an automated hematoma segmentation and classification based on a weighted grayscale histogram feature in a hierarchical classification structure.[13] However, this did not address the challenging problem of edema segmentation. Supervised learning methods such as convolutional neural networks (CNN) have been used to segment tumor tissue in MRI scans.[14] However, for our problem, the size of the training data is often small ($n \approx 30$), and the subjectivity of the manual training data would be a disadvantage.

Our unsupervised method has two stages. For the hematoma segmentation stage, we first use a nonlocal regularized spatial fuzzy C-means (FCM) to segment an approximate contour of the hematoma, and then we use the active contours without edges (ACWEs) method to refine the contour. For the edema segmentation stage, we first initialize the region using the tissue surrounding the hematoma, since the edema is usually a surrounding ring-shaped region, and then we use the ACWE method again on either a smaller region of interest (ROI) or a modified image to obtain the final contour. The rest of the paper is organized as follows. Section 2 introduces the hematoma and edema segmentation process in detail. Section 3 gives our experimental results based on real data, and Section 4 provides a discussion and conclusion.

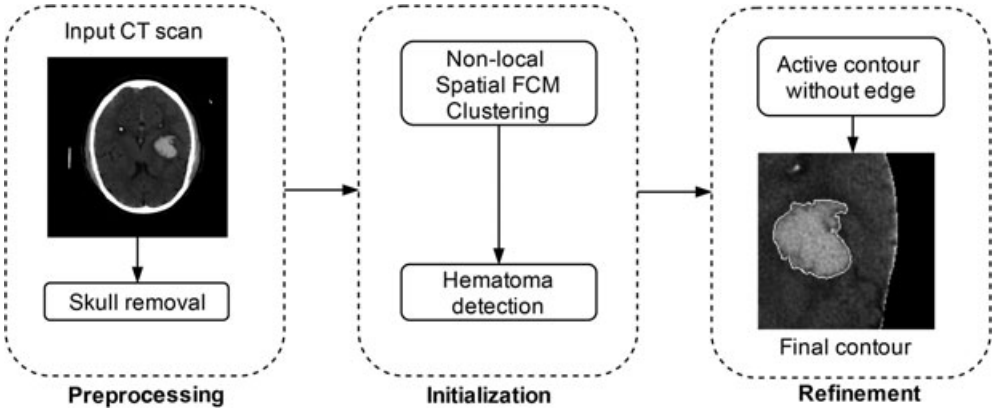

FIGURE 2 Flowchart for hematoma segmentation process. CT, computed tomography; FCM, fuzzy C-means

2 | METHOD

The segmentation framework has two stages: hematoma segmentation and edema segmentation. Hematoma is a localized collection of blood outside the blood vessels, so it has a higher density and appears brighter than other tissues. The hematoma segmentation step first performs a fuzzy clustering. Since the objects have a clear spatial pattern in CT scans, we add a spatial penalty to the energy function. We also add a nonlocal regularization term to deal with image noise and artifacts. We then apply the ACWE method using the clustering result as the initial contour. For the edema segmentation, we set the initial contour to the region surrounding the segmented hematoma tissue and then apply the ACWE method.

2.1 | Hematoma segmentation

Figure 2 gives a flowchart of the hematoma segmentation. There are three steps: the preprocessing step including a simple skull removal, the initialization step using nonlocal regularized spatial FCM clustering, and the refinement step using ACWE.

The input CT images are in DICOM (Digital Imaging and Communications in Medicine) format and did not undergo preprocessing. They were constrained to values between -1024 and 3071 Hounsfield units (HU). We applied a simple and fast skull removal as follows. First, each image is thresholded using the brain tissue range (0-100 HU), and pixels outside this range are set to 0 HU. We retain the largest connected component from the thresholded image and discard any isolated small objects. The initialization step uses nonlocal regularized spatial FCM,[15,16] and we now give the technical details.

Nonlocal regularized spatial FCM: Let Ω be a bounded subset of $\mathbb{R}^2$ and $u_0 : \Omega \to \mathbb{R}$ be a given image. Our task is to segment the image u_0 into $K\,(\geq 2)$ classes. Standard FCM can be defined as the minimization of the following energy function:

$$J_{\mathrm{FCM}} = \sum_{j\in\Omega}\sum_{k=1}^{K} u_{jk}^{q}(y_j - v_k)^2,$$

where y_j is the gray-level value at pixel j, v_k is the mean gray-level value in class k, and $(u_{jk})_{k=1}^{K} = (u_{j1}, u_{j2}, \ldots, u_{jK})$ are the membership ratios of pixel j with respect to these K classes such that $\sum_{k=1}^{K} u_{jk} = 1$ and $u_{jk} \in [0,1]$. Parameter $q > 1$ controls the degree of fuzziness: the membership functions become increasingly fuzzy as q increases. To use the spatial structure information of the image, we add a spatial penalty term to the energy function:

$$J_{\mathrm{SFCM}} = \sum_{j\in\Omega}\sum_{k=1}^{K} u_{jk}^{q}(y_j - v_k)^2 + \frac{\rho}{2}\sum_{j\in\Omega}\sum_{k=1}^{K} u_{jk}^{q}\sum_{n\in N_j}\sum_{l\in L_k} u_{nl}^{q},$$

where N_j is the set of neighbors of pixel j, $L_k = \{1 : K\} \setminus \{k\} = \{1, \ldots, k-1, k+1, \ldots, K\}$, and the parameter ρ controls the trade-off between the data term and the spatial regularization term. Furthermore, to improve the algorithm's robustness to image noise and artifacts, we add to the energy function a nonlocal weight function that measures the

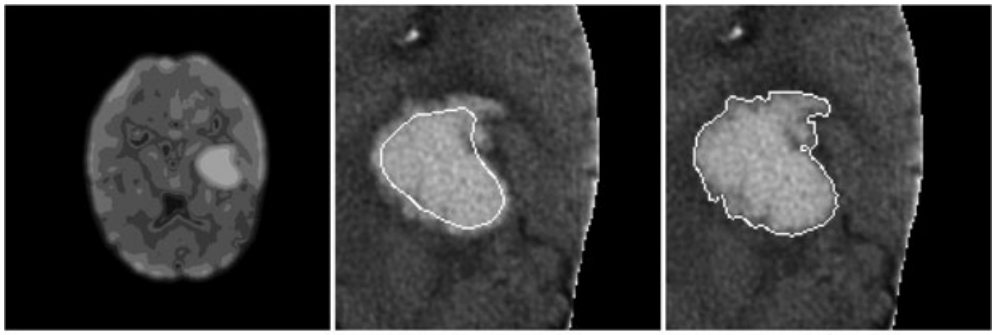

FIGURE 3 Clustering results. A, Each grayscale level in the graph represents a cluster and $K = 8$; B, Initial hematoma contour; C, Final hematoma contour

similarity of two pixels. Nonlocal regularized spatial FCM can be defined as the minimization of the following energy function:

$$J_{\text{NL-SFCM}} = \sum_{j\in\Omega}\sum_{k=1}^{K}\sum_{n\in N_j} w_{jn}u_{jk}^{q}(y_j - v_{kn})^2 + \frac{\rho}{2}\sum_{j\in\Omega}\sum_{k=1}^{K}u_{jk}^{q}\sum_{n\in N_j} w_{jn}\sum_{l\in L_k} u_{nl}^{q},$$

where v_{kn} is the mean gray-level value in class k over a local neighborhood denoted N_n.The weight w_{ij} measures the similarity of two pixels by comparing their neighborhoods: $w_{ij} = Z_i^{-1}\exp(-1/h^2\|y(P_i) - y(P_j)\|_2^2)$, where $y(P_i)$ is a vector containing the gray-level values in the neighborhood of pixel i, Z_i is a normalization constant, and h is a smoothing parameter. The minimization problem can be solved using a gradient-based method, and more details can be found in.[16]

We scale the whole image to [0, 1] and apply the nonlocal spatial FCM clustering algorithm. The number of clusters K must be large enough to cover the different types of tissue appearing in the image: background, gray matter (GM), white matter (WM), cerebrospinal fluid, hematoma, edema, some remaining skull, and others. Thus, K should be larger than 7, and we use $K = 8$ for the experiments in this study. We find that a larger K gives a more detailed segmentation of GM and WM without greatly affecting the hematoma result. We set N_j to a 3×3 square centered in pixel j and the fuzziness parameter $q = 2$. We used 10-fold cross-validation to determine the tuning parameter ρ, and the cross validation error is defined to be the data term (first term) in $J_{\text{NL-SFCM}}$. An example of the clustering results is shown in Figure 3A, and the original scan is in the left panel of Figure 1. Each different grayscale level in the image represents a different cluster, and we can see that the segmented clusters are all spatially well defined and the hematoma tissue has been segmented out successfully.

To determine whether or not an image contains hematoma, we compare the cluster that has the largest mean gray-level value with a predefined threshold. This is because hematoma has a much higher density than other tissue since it is mostly a localized collection of blood outside blood vessels. In the experiments we use a threshold of 40 HU because blood usually has an HU of about 40. We also computed the average hematoma density in the manual segmentation results, and 40 is a consistent cutoff between hematoma and other tissues. However, it should be noted that a simple threshold-based method would not work well because of the complex structure and heterogeneity in the CT images.

The nonlocal regularization term in the clustering step helps us to deal with image noise and inhomogeneity artifacts, but it also indirectly smooths the image, blurring the boundaries of the objects. In Figure 3B, the initial contour acquired by clustering is smaller than the actual contour. The spatial penalty term does not guarantee that the selected clusters are all spatially connected. To improve the accuracy of the algorithm, we use ACWE[17] for the second stage of the hematoma segmentation. We use the clustering result as the initial contour. We will discuss the ACWE model in the next section since it is the main tool for edema segmentation. Figure 3C shows an example of a final contour.

2.2 | Edema segmentation

Edema segmentation is a more challenging task than hematoma segmentation because of the subtle difference between edema and the surrounding healthy tissue. Edema is a secondary injury that appears after hematoma, and it usually forms a ring-shaped region surrounding the hematoma. Since the edema boundary is often not well defined, there is in

general no ground truth, and the manual segmentation results show a large inter and intrarater variation. Gradient-based techniques do not work well because of the subtle differences in the intensity values. To overcome these limitations, we use the ACWE method proposed by Chan and Vese,[17] which is suitable for images with relatively smooth intensity fluctuations and does not depend on the gradient map for the algorithm to converge. We now introduce the method.

Active contours without edges: The basic idea in an ACWE model is to evolve a curve, subject to the constraints from the given image u_0, to detect objects in that image. The curve starts close to the object to be detected, moves toward its interior normal, and stops on the boundary of the object. Let us define the evolving curve C in Ω as the boundary of an open subset w of Ω. In a simple case, the final contour is reached by minimizing the energy function:

$$\begin{aligned} F(c_1, c_2, C) = \mu \cdot \text{Length}(C) + \nu \cdot \text{Area}(\text{inside}(C)) \\ + \lambda_1 \int_{\text{inside}(C)} |u_0(x,y) - c_1|^2 dx \quad dy \\ + \lambda_2 \int_{\text{outside}(C)} |u_0(x,y) - c_2|^2 dx \quad dy, \end{aligned}$$

where $u_0(x,y)$ is the gray-level value at the pixel with coordinate (x,y); c_1, c_2 are the averages of u_0 inside C and outside C; and $\mu \geq 0, \nu \geq 0, \lambda_1, \lambda_2 > 0$ are fixed parameters. In all our experiments, we fix $\mu = \lambda_1 = \lambda_2 = 1$ and $\nu = 0$. The first two terms of the energy function control the regularity of the curve, and the last two terms create homogenous regions. The evolving curve $C \in \Omega$ can be formulated using the level set method[18] as the zero level set of a Lipschitz function $\phi : \Omega \to \mathbb{R}$. Then, the energy $F(c_1, c_2, \phi)$ can be written as

$$\begin{aligned} F(c_1, c_2, \phi) = \mu \int_\Omega \delta(\phi(x,y)) |\nabla \phi(x,y)| dx \quad dy + \nu \int_\Omega H(\phi(x,y)) dx \quad dy \\ + \lambda_1 \int_\Omega |u_0(x,y) - c_1|^2 H(\phi(x,y)) dx \quad dy \\ + \lambda_2 \int_\Omega |u_0(x,y) - c_2|^2 (1 - H(\phi(x,y))) dx \quad dy, \end{aligned}$$

where H is the Heaviside function and $\delta = \frac{d}{dz} H(z)$ is the Dirac measure. To compute the associated Euler-Lagrange equation for the unknown function ϕ, we consider slightly regularized versions of the function H and δ, denoted H_ϵ and δ_ϵ. Different ways can be used to regularize H, and in our experiments, $H_\epsilon(z) = \frac{1}{2}(1 + \frac{2}{\pi} \arctan(\frac{z}{\epsilon}))$ is used, and $\delta_\epsilon = H'_\epsilon$. Replace H and δ in $F(c_1, c_2, \phi)$ by H_ϵ and δ_ϵ, we obtain $F_\epsilon(c_1, c_2, \phi)$. Keeping c_1 and c_2 fixed, we minimize F_ϵ with respect to ϕ to obtain the associated Euler-Lagrange equation for ϕ. If we parameterize the descent direction by an artificial time $t \geq 0$, the equation in $\phi(t,x,y)$ (with $\phi(0,x,y) = \phi_0(x,y)$) defining the initial contour is

$$\begin{aligned} \frac{\partial \phi}{\partial t} = & \delta_\epsilon(\phi) \left[\mu \text{div} \left(\frac{\nabla \phi}{|\nabla \phi|} \right) - \nu - \lambda_1 (u_0 - c_1)^2 + \lambda_2 (u_0 - c_2)^2 \right] = 0 \\ & \text{in} \quad (0, \infty) \times \Omega, \phi(0,x,y) = \phi_0(x,y) \quad \text{in} \quad \Omega, \frac{\delta_\epsilon(\phi)}{|\nabla \phi|} \frac{\partial \phi}{\partial \vec{n}} = 0 \quad \text{on} \quad \partial\Omega, \end{aligned}$$

where $\text{div}(v)$ is the divergence of vector v, $\vec{n}$ denotes the exterior normal to the boundary $\partial\Omega$, and $\frac{\partial \phi}{\partial \vec{n}}$ denotes the normal derivative of ϕ at the boundary.

Since the CT scans in our problem have a more complicated structure than just an object and the background, a different initial contour may lead to a different result. Ideally, the initial contour should be around the object to be detected. For the refinement step of the hematoma segmentation, since the hematoma tissue is quite obvious and the clustering result is a good approximation of the actual contour of the hematoma tissue, the ACWE method can easily converge to the final contour by using the clustering result as the initial contour $\phi_0(x,y)$. Figure 3C shows an example of applying the ACWE method to the initial contour in Figure 3B.

For edema segmentation, we use the region surrounding the segmented hematoma as the initial contour. In the experiments, this is achieved through image dilation. A spherical structuring element with a radius of R pixels is created using the boundary of the segmented hematoma, and only the region outside the hematoma is selected. Figure 4A shows an example of dilation, with $R = 5$ pixels. However, simply choosing a different initial contour will not lead to convergence to the edema contour because the ACWE model assumes that the image u_0 is formed of two regions of approximately piecewise-constant intensities. The hematoma is much clearer than the edema, so the model will converge to the final contour of the hematoma even though the initial contour is the surrounding region. To make the edema clearer, we propose

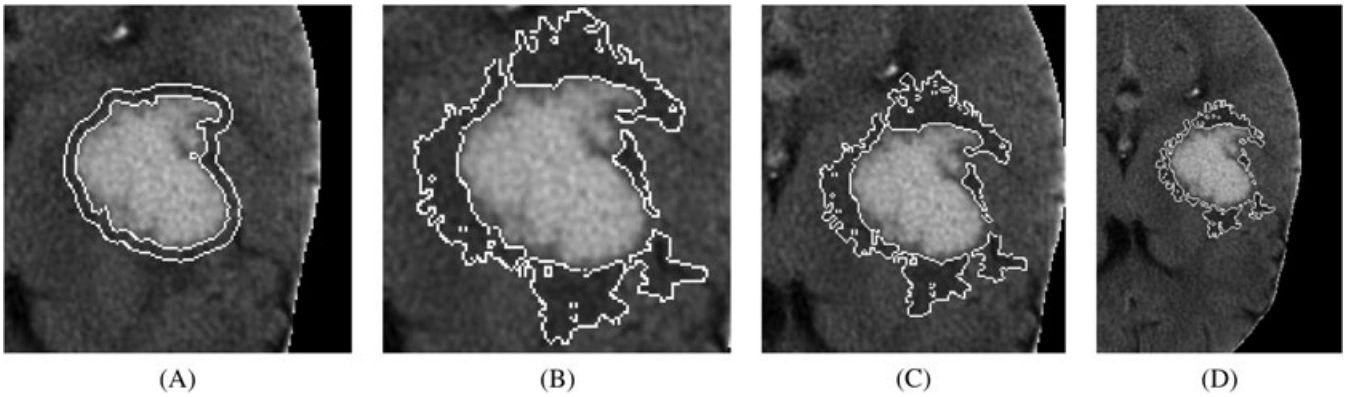

FIGURE 4 (A) Initial contour of edema segmentation based on the dilation of hematoma contour; (B), (C), (D) Final contour of the edema using three different region of interest sizes

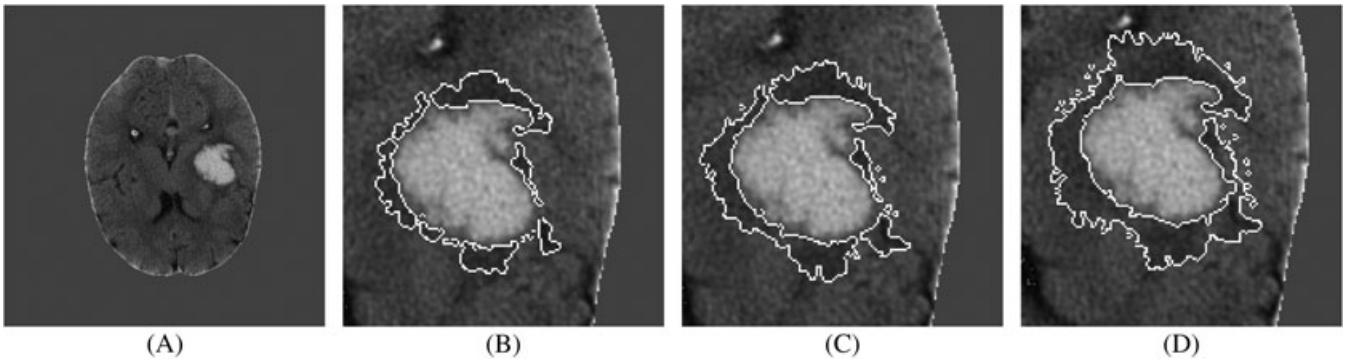

FIGURE 5 (A) Modified image after replacing the background with the brain average; (B), (C), (D) Final edema contour with $R = 5$, 10, and 20 pixels, respectively. Note that the active contours without edge method is applied to the full image

two approaches. First, instead of working with the full image, we can work with a smaller ROI with a simpler structure. However, this needs some manual intervention. Figures 4B to 4D show the results of applying ACWE to three different ROI sizes when the initial contour is chosen as the area dilated from the hematoma boundary with a radius of 5 pixels. We can see that the segmentation results are not very sensitive to the choice of ROI, provided it is sufficiently local to cover all the tissue of interest.

Second, we can avoid the need for human intervention in the choice of ROI by working with the full image. ACWE converges to the hematoma because of the strong contrast between the hematoma (bright) and the background (dark). To remove this effect, we substitute the background (0 HU) with the average of the brain tissue (usually, around 30 HU, depending on the image). Figure 5A shows the resulting image. We then apply ACWE, and the initial contour is again chosen as the region surrounding the hematoma. An alternative is to cut the background and work only with the brain tissue. These two methods give similar results. To illustrate the effect of the size of the initial contour, Figures 5B to 5D show the results for $R = 5$, 10, and 20 pixels, respectively. Note that ACWE is applied to the full image so there is no need to choose an ROI; the enlarged images simply give a better illustration of the final contour. We can see that the results are not very sensitive to the size of the dilation, and all three images provide a fairly accurate segmentation result for the edema. We used $R = 5$ pixels for all the experiments reported in Section 3.

3 | EXPERIMENTS

We tested our method on a sample of 30 patients and compared our results with the manual segmentation results. The patients were 18 years of age or older, with an average age of 69.77 years. Of the 11 female and 19 male subjects, 13 have ICH in the left hemisphere and 17 in the right hemisphere. The location of the ICH was the lentiform ($n = 13$), lobar ($n = 8$), thalamus ($n = 5$), caudate ($n = 2$), or putamen ($n = 2$).

TABLE 1 Sensitivity and dice score coefficient (DSC) of hematoma and edema for the two raters

	Hematoma		Edema	
	Sensitivity	DSC	Sensitivity	DSC
Mean	0.93	0.93	0.71	0.64
S.D.	0.01	0.02	0.12	0.08
Min	0.84	0.89	0.47	0.42
Max	1.00	1.00	0.91	0.77

TABLE 2 Sensitivity and dice score coefficients comparing manual tracing and automated segmentation of brain hematoma and edema for each rater

Rater 1	Hematoma		Edema		Rater 2	Hematoma		Edema	
	Sensitivity	DSC	Sensitivity	DSC		Sensitivity	DSC	Sensitivity	DSC
Mean	0.92	0.92	0.64	0.57		0.92	0.92	0.60	0.58
S.D.	0.07	0.05	0.13	0.11		0.07	0.05	0.15	0.10
Min	0.75	0.82	0.30	0.35		0.76	0.81	0.27	0.29
Max	0.99	0.97	0.85	0.71		0.99	0.96	0.92	0.70

Abbreviations: DSC, dice score coefficient.

Most of the CT scans were acquired in hospital emergency rooms, and each slice is a 512 × 512 matrix with a thickness of 5 mm. The number of slices varies from 26 to 32 among the subjects. For each subject, the damaged area was manually measured by two independent radiological experts (raters A and B) and automatically segmented by our method. The experts independently traced the hematoma and edema outlines on each of the CT slices. Our segmentation framework was also applied to each slice independently; no interpolation was done between slices.

To compare the automated and manual results, we classify the pixels into four groups: true positives (TPs), ie, hematoma pixels found by both the automated and manual methods; false positives (FPs), ie, hematoma pixels found only by the automated method; false negatives (FNs), ie, hematoma pixels found only by the manual method; and true negatives (TNs), ie, ordinary pixels found by both methods. We used the same classification for the edema segmentation. To compare the results, we use two measures: the sensitivity and the dice score coefficient (DSC). They are computed as follows:

$$\text{Sensitivity} = \frac{n_{\text{TP}}}{n_{\text{FN}} + n_{\text{TP}}}, \qquad \text{and} \qquad \text{DSC} = \frac{2n_{\text{TP}}}{n_{\text{FN}} + 2n_{\text{TP}} + n_{\text{FP}}}.$$

The sensitivity is the direct ratio of the TPs to the total number of positive pixels in the manual results. The DSC also measures the similarity levels of the two regions, and it adds a penalty for FPs. For both measures, a value of 0 indicates no overlap between two areas, and 1 indicates a perfect match. For each subject, the sensitivity and DSC are calculated by combining all the slices, and this is done separately for the hematoma and edema. For the edema segmentation, we replaced the background with the average of the brain tissue to avoid human intervention.

First, to measure the reliability of the two raters, we compute the sensitivity and DSC of rater B compared to rater A, so rater A is considered to be the gold standard. Table 1 gives the summary statistics for the two raters. For the hematoma, both measures have an average similarity greater than 0.9. However, for the edema, the average DSC is only 0.64, and it can be as low as 0.42 for some subjects. Table 2 gives the summary statistics of similarity measures for the automated and manual results. For hematoma segmentation, our automated algorithm gives excellent results. The sensitivity and DSC are above 0.9 for both raters, and the poorest performance is 0.75 for sensitivity and 0.82 for DSC. For edema segmentation, the performance of our algorithm is comparable with the manual results. The average sensitivity is over 0.60, which is only slightly smaller than the 0.71 for the two raters. Overall, the proposed framework for hematoma and edema segmentation provides objective and reproducible results that are close to the manual results. The process is also fully automated, and the processing time for each subject is about 5 minutes.

4 | CONCLUSION AND DISCUSSION

The ICH is a major cause of morbidity and mortality in stroke patients. Quantification of the hematoma and edema volume helps physicians to determine the appropriate treatment. The relative edema volume can also be used as a potential predictor of the 30-day mortality rate and the functional outcome. The manual segmentation of hematoma and edema from CT scans is time consuming and labor intensive; an automated algorithm can provide accurate and objective results. There is limited literature addressing this problem, and we have proposed an automated method to segment brain hematoma and edema from CT scans. We use nonlocal regularized spatial FCM clustering and ACWE. Our approach has excellent performance in hematoma segmentation; the DSC is above 90% compared with the manual results. Although edema segmentation lacks a gold standard because of the poorly defined boundary between the edema and the surrounding tissue, our method was comparable with the results of two independent raters. It is also worth mentioning that the process is fully automated and takes less than five minutes per subject.

In this study, all segmentations are done in 2D. The thickness of CT scans is usually only about 5 mm, and there is continuity between slices. Extra information could be gained by combining the slices and performing 3D segmentation. The nonlocal spatial FCM and the ACWE could be generalized to 3D. This would be an interesting direction for further research. Furthermore, the FCM-based methods used here can also be applied to other areas such as document analysis,[19] automatic number plate recognition,[20] and supply chain management,[21] and Nayak et al[22] provides a comprehensive review on these possible applications.

ACKNOWLEDGEMENTS

The authors wish to thank two reviewers for their helpful comments and suggestions that led to substantial improvements in the article. Sincere thanks also go to the Editor-in-Chief, Professor Fabrizio Ruggeri, and the guest editor of the "High-Dimensional Data Analysis" special issue, Professor Ejaz Ahmed. This work was supported by the Natural Sciences and Engineering Research Council of Canada. Linglong Kong's research was also supported by the Canadian Statistical Sciences Institute.

DECLARATION OF CONFLICTING INTERESTS

The author(s) declared no potential conflicts of interest with respect to the research, authorship, and/or publication of this article.

REFERENCES

1. Qureshi AI, Tuhrim S, Broderick JP, Batjer HH, Hondo H, Hanley DF. Spontaneous intracerebral hemorrhage. *N Engl J Med*. 2001;344(19):1450-1460.
2. Zhang LF, Yang J, Hong Z, et al. Proportion of different subtypes of stroke in China. *Stroke*. 2003;34(9):2091-2096.
3. Flaherty ML, Haverbusch M, Sekar P, et al. Long-term mortality after intracerebral hemorrhage. *Neurology*. 2006;66(8):1182-1186.
4. Broderick JP, Adams Jr HP, Barsan W, et al. Guidelines for the management of spontaneous intracerebral hemorrhage. *Stroke*. 1999;30(4):905-915.
5. Broderick JP, Brott TG, Duldner JE, Tomsick T, Huster G. Volume of intracerebral hemorrhage. A powerful and easy-to-use predictor of 30-day mortality. *Stroke*. 1993;24(7):987-993.
6. Gebel Jr JM, Jauch EC, Brott TG, et al. Natural history of perihematomal edema in patients with hyperacute spontaneous intracerebral hemorrhage. *Stroke*. 2002;33(11):2631-2635.
7. Gebel Jr JM, Jauch EC, Brott TG, et al. Relative edema volume is a predictor of outcome in patients with hyperacute spontaneous intracerebral hemorrhage. *Stroke*. 2002;33(11):2636-2641.
8. Appelboom G, Bruce SS, Hickman ZL, et al. Volume-dependent effect of perihaematomal oedema on outcome for spontaneous intracerebral haemorrhages. *J Neurol Neurosurg Psychiatry*. 2013;84(5):488-493.
9. Zimmerman RD, Maldjian JA, Brun NC, Horvath B, Skolnick BE. Radiologic estimation of hematoma volume in intracerebral hemorrhage trial by CT scan. *Am J Neuroradiol*. 2006;27(3):666-670.
10. Gordillo N, Montseny E, Sobrevilla P. State of the art survey on MRI brain tumor segmentation. *Magn Reson Imaging*. 2013;31(8):1426-1438.
11. Lončarić S, Dhawan AP, Kovačević D, Ćosić D, Broderick J, Brott T. Quantitative intracerebral brain hemorrhage analysis. In: Proceedings of the Medical Imaging; 1999; San Diego, CA.
12. Bardera A, Boada I, Feixas M, et al. Semi-automated method for brain hematoma and edema quantification using computed tomography. *Comput Med Imaging Graph*. 2009;33(4):304-311.

13. Shahangian B, Pourghassem H. Automatic brain hemorrhage segmentation and classification algorithm based on weighted grayscale histogram feature in a hierarchical classification structure. *Biocybern Biomed Eng*. 2016;36(1):217-232.
14. Havaei M, Davy A, Warde-Farley D, et al. Brain tumor segmentation with deep neural networks. *Med Image Anal*. 2017;35:18-31.
15. Pham DL. Spatial models for fuzzy clustering. *Comput Vis Image Underst*. 2001;84(2):285-297.
16. Caldairou B, Passat N, Habas PA, Studholme C, Rousseau F. A non-local fuzzy segmentation method: application to brain MRI. *Pattern Recognit*. 2011;44(9):1916-1927.
17. Chan TF, Vese LA. Active contours without edges. *IEEE Trans Image Process*. 2001;10(2):266-277.
18. Osher S, Sethian JA. Fronts propagating with curvature-dependent speed: algorithms based on Hamilton-Jacobi formulations. *J Comput Phys*. 1988;79(1):12-49.
19. Yan Y, Chen L, Tjhi WC. Fuzzy semi-supervised co-clustering for text documents. *Fuzzy Sets Syst*. 2013;215:74-89.
20. Chang SL, Chen LS, Chung YC, Chen SW. Automatic license plate recognition. *IEEE Trans Intell Transp Syst*. 2004;5(1):42-53.
21. Yin XF, Khoo LP, Chong YT. A fuzzy c-means based hybrid evolutionary approach to the clustering of supply chain. *Comput Ind Eng*. 2013;66(4):768-780.
22. Nayak J, Naik B, Behera HS. Fuzzy c-means (FCM) clustering algorithm: a decade review from 2000 to 2014. *Computational Intelligence in Data Mining - Volume 2: Proceedings of the International Conference on CIDM, 20-21 December 2014*. Berlin, Germany: Springer; 2015:133-149.

How to cite this article: Tu W, Kong L, Karunamuni R, Butcher K, Zheng L, McCourt R. Nonlocal spatial clustering in automated brain hematoma and edema segmentation. *Appl Stochastic Models Bus Ind*. 2019;35:321–329. https://doi.org/10.1002/asmb.2431